· Effect of EMBr on Multiphase Flow and Bubble Entrapment in Steel Continuous Casting

JIN Kai[1], THOMAS Brian G.[1], RUAN Xiao-ming[2]

(1. Dept. of Mechanical Science and Engineering, University of Illinois at Urbana–Champaign, Urbana, IL, USA;

2. Steelmaking Research Department, Research Institute, Baoshan Iron & Steel Co., Ltd., Shanghai, P. R. China）

Abstract: In steel continuous casting, double-ruler electromagnetic braking (EMBr) is often applied to control the flow pattern in the mold. In addition, argon gas is usually injected to prevent clogging, but the bubbles also affect the flow pattern, and may become entrapped to form defects in the final product. To investigate the combined behaviors, plant measurements were conducted and a computational model was applied to simulate turbulent flow of the molten steel and the transport and capture of argon gas bubbles into the solidifying shell in a continuous slab caster, including EMBr. An Eulerian k-ε model of the steel flow was two-way coupled with a Lagrangian model of the large bubbles using a Discrete Random Walk method to simulate their turbulent dispersion. The top surface velocities agreed well with nailboard measurements, and indicated strong cross flow caused by biased flow of Ar gas due to the slide-gate orientation. Then, the trajectories and capture of over two million bubbles (25 μm to 5 mm diameter range) were simulated using an advanced capture criterion. The number, locations, and sizes of captured bubbles agreed well with measurements, especially for larger bubbles. The relative capture fraction of 0.3% was close to the measured 0.2% for 1mm bubbles, and occurred mainly near the top surface. About 85% of smaller bubbles were captured, mostly deeper down in the caster. EMBr produced similar behavior with slightly lower capture rates.

Key words: continuous casting, bubble entrapment, computational model, model validation, EMBr

1 Introduction

An Electromagnetic Breaking (EMBr) system is often used in the continuous casting (CC) process to alter the molten steel flow pattern. A static (direct-current) magnetic field through the thickness direction of the mold generates current in the conducting steel, which induces a Lorentz force that pushes on the molten steel and modifies the flow pattern. Argon gas is usually injected at the slide gate or stopper rod to prevent nozzle clogging. [1] The jets of molten steel then carry those bubbles through the Submerged Entry Nozzle (SEN) and into the mold cavity region, where they greatly affect the flow pattern, surface level fluctuations, and slag entrainment. Large bubbles captured near the surface can lead to blister defects, such as pencil pipe, after rolling and annealing. [2] Furthermore, the moving Ar bubbles collect nonwetting inclusion particles, such as alumina. If such a bubble is captured by the solidifying steel shell, the layer of inclusions covering its surface will lead to large oxide clusters, which cause severe sliver defects in the final product. [3]

The modeling of ruler-shaped EMBr effect on fluid flow in the CC process has been studied by several researchers [4–6]. Usually, the molten steel flow is more stable and surface velocities are slower with the magnetic field [5,6]. The magnetic field can also suppress turbulence. [4–6] Previous models of two-phase Ar and steel flow in continuous casting have used different methods [6–8] to achieve the necessary two-way coupling to predict the flow pattern, and reveal the importance of the larger bubbles.

THOMAS Brian G., Professor; **E-mail:** bgthomas@illinois.edu

To predict the capture fraction and location of different-sized Ar bubbles/particles, a suitable capture criterion is needed. A "simple" capture criterion (particles are entrapped if they touch the solidification front) is often used. [9–11] Yuan, Mahmood and Thomas [9,10,12] developed an "advanced" particle capture criterion based on a local force balance on particles reaching the solidification front. This model includes the effects of particle size, Primary Dendrite Arm Spacing (PDAS), concentration gradient forces and other effects. This capture criterion was successfully validated with previous measurements [8], so is used in the current study.

A few studies [8,9,12] have investigated quantitatively the capture fraction and distribution of inclusion particles in continuous casting. Yuan et al. [9] performed particle capture simulations for small bubbles (less than 40μm) in a thin-slab steel caster using Large Eddy Simulation (LES) where the effect of transient local turbulent eddies on particle transport was automatically included. A removal rate of 8% of small inclusions was predicted, independent of both particle size and density, which suggests that the particles were too small to deviate significantly from the surrounding fluid flow. Computationally effective RANS models with a Discrete Random Walk (DRW) method [13] to mimic the dispersion of bubbles due to turbulence were also developed. [8,11] Using a k-ε flow model with both simple and the force balance capture criterion [9,10,12], Jin et al. [8] studied the capture of argon gas bubbles in a commercial caster. The removal fraction exceeded 99.9% for large argon bubbles (>1mm) and ~16% for small bubbles (<0.1mm). The advanced force balance criterion agreed better with measurements than the simple criterion. Using a k-ε flow model, solidification heat transfer with the solid shell, and the simple capture criterion, Wang and Zhang [11] predicted transport and entrapment of small inclusions in the full length of a billet caster. Most 5 μm inclusions were captured deep in the strand.

The effect of EMBr on argon bubble transport and capture has not been well studied. This work investigates the capture of argon bubbles in a commercial caster with three different magnetic field configurations.

2 Plant measurements

Plant measurements of the magnetic fields, molten steel flow and bubble entrapment were conducted on the No. 4 caster at Baosteel, Shanghai in 2012. Top surface velocities of this conventional (230×1300 mm) continuous steel slab caster were measured with two sets of nailboard dipping tests [14]. Casting conditions and process parameters are given in table 1. Flow rate of the molten steel through the SEN into the mold is controlled by a slide-gate that moved between the geometric center and the Inside Radius (IR) side of the caster. For the experiments casting 1300mm wide slabs at 1.5m/min, the slide gate was 70% open, as shown in figure 1(a). The measured magnetic field strengths down the mold are shown in figure 1(b).

Table 1. Process parameters

Process Parameters	Value
Mold thickness (L_t)	230 mm
Mold width (L_w)	1300 mm
Casting speed (V_c)	1.5 m/min
Argon volume fraction (α)	8.2 vol%
Steel density (ρ)	7000 kg/m^3
Argon density (ρ_p)	0.5 kg/m^3
Steel viscosity (μ)	6.30×10^{-3} kg/(m·s)
Ar viscosity (μ_p)	2.12×10^{-5} kg/(m·s)

To investigate the capture of Ar bubbles during the process for the conditions in table 1, samples were cut from the center and quarter of the Wide Face (WF), and Narrow Face (NF) of the steel slab. The sample locations and sizes are shown in figure 1(c). To quantify the number and location of the bubbles captured in the samples, the outer 3 mm of the surface of each sample was milled away, and then a 35x optical microscope was used to record the diameter of each bubble observed on the exposed surface, and the number of bubbles in each size range was counted. After recording the results, another 3mm steel was milled away and the bubbles on the new exposed surface were measured. This procedure was repeated to examine six layers total, located at 3, 6, 9, 12, 17 and 22 mm beneath slab outer surface. The polished sample surface is unlikely to cut through captured bubbles at their largest center diameter. Thus, the visible circle diameters are usually smaller than the real sphere diameters. A simple method proposed by Lekakh et al. [15] was used here to convert the observed diameters into realistic diameters of the spherical bubbles, and presented in the results.

$$d_{true} = d_{visible} / 0.785 \qquad (1)$$

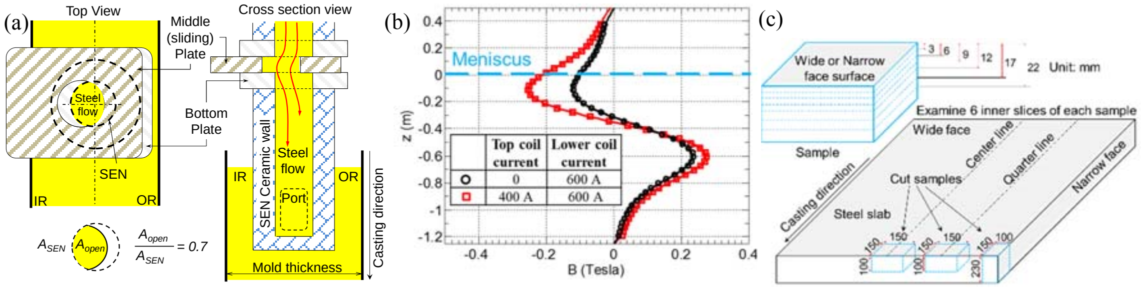

Fig. 1 (a) Slide gate configuration; (b) Magnetic field distribution; (c) Samples and six examined surfaces;

3 Computational models and solution procedure

A three-dimensional finite-volume computational model together with Lagrangian particle tracking was applied to study the flow behavior and the transport phenomena of Ar bubbles in the caster. First, a steady-state solution of single-phase flow of molten steel was obtained using the standard *k-ε* model. Then, based on that solution, a RANS and Lagrangian Discrete Phase Model (DPM) coupled simulation was used to predict pseudo steady flow, including the effect of Ar gas. The DRW model was used to include the effect of turbulence on bubble dispersion, and buoyancy of the large gas bubbles affects the liquid momentum equation. After obtaining the multiphase flow field, many Ar bubbles of different sizes were injected at the SEN inlet to study the transport and capture of the bubbles. A capture criterion [9,10,12] based on a force balance at the interface was implemented into ANSYS FLUENT [16] using User Defined Functions (UDFs).

•

3.1 Bubble size distribution

In this study, the volume distribution of the Ar bubbles was assumed to obey a Rosin-Rammler [17] distribution, which was originally used to describe solid particle distributions. The ideal Rosin-Rammler cumulative distribution *F(d)* is defined by the mean diameter d_{mean} and spread parameter η.

$$F(d_i) = 1 - \exp\left(-d_i / d_{mean}\right)^{\eta} \qquad (2)$$

In this work, a discrete form of this distribution function (with d_{mean}=3 and η=4) was used with 11 different bubble sizes, d_i, where i is the bubble size group, and $F(d_i)$ is the volume fraction of Ar contained in those bubbles with diameter less than d_i. The blue squares in figure 2(a) are a histogram of the volume fraction and diameter of each group of bubbles. The red staircase line sums these volume fractions. Note that the ideal Rosin-Rammler distribution (black dashed line) passes through the cumulative line of the discrete points. Note also that less than 1% of the bubbles have diameter less than 1 mm.

3.2 Two-way coupled argon-steel flow model

The computational domain contains half of the slide-gate, SEN and mold region (from mold surface to 2.5 m below meniscus). The mesh had ~1 million hexahedral finite-volume cells as shown in figure 2(b). A single-phase flow simulation provided an initial guess for the later two-way coupled steel-Ar flow simulation.

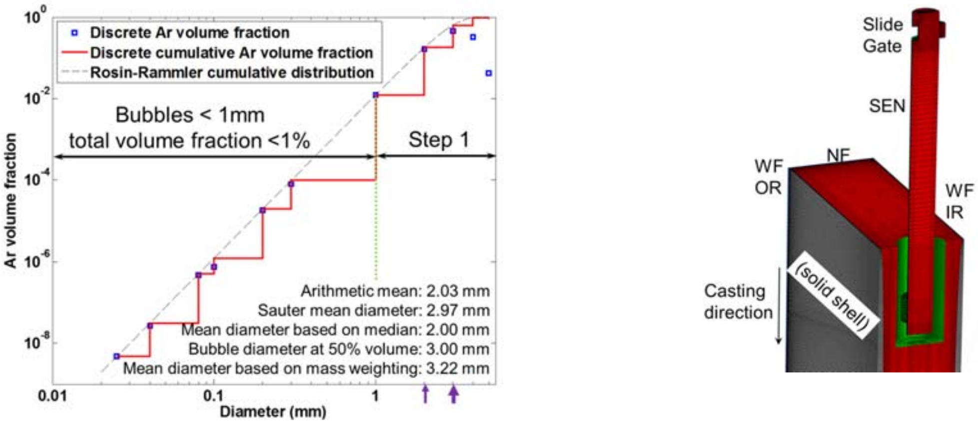

Fig. 2 (a) Ar bubble volume fraction distribution and (b) Mesh of the computational domain

The solid shell was included in this domain with thickness found by $s(mm) = 3[t(s)]^{1/2}$. The solid shell is modeled as an electrical conduction zone where the fluid flow equations are not solved. The continuity and momentum equations for liquid steel are:

$$\nabla\cdot(\rho\boldsymbol{U}) = S_{\text{mass-sink}} \tag{3}$$

$$\rho\frac{\partial\boldsymbol{U}}{\partial t} + \rho(\boldsymbol{U}\cdot\nabla)\boldsymbol{U} = -\nabla\left(\bar{p} + \frac{2}{3}\rho k\right) + \nabla\cdot\left[(\mu+\mu_t)\nabla\boldsymbol{U}\right] + \boldsymbol{S}_{\text{momentum-sink}} + \boldsymbol{S}_{\text{DPM}} + \boldsymbol{S}_{EMBr} \tag{4}$$

In the two-way coupled simulation step, the source term $\boldsymbol{S}_{\text{DPM}}$ in equation (4) was taken from the DPM model to include the drag of each rising bubble acting on the local fluid. Mass and momentum sinks were added near the shell through UDFs to include the effect of the solidifying shell, as explained elsewhere[10]. The k-ε model was used to model turbulence[18]. The Lorentz force source $\boldsymbol{S}_{\text{EMBr}}$ was solved using the potential method. By defining an electric potential Φ, the current density $\boldsymbol{J}$ can be computed through Ohm's law:

$$\boldsymbol{J} = \sigma\left(-\nabla\Phi + \boldsymbol{u}\times\boldsymbol{B}\right) \tag{5}$$

Due to current conservation, the electric potential Φ for a conducting fluid satisfies

$$\nabla\cdot(\sigma\nabla\Phi) = \nabla\cdot\left[\sigma(\boldsymbol{u}\times\boldsymbol{B})\right] \tag{6}$$

The Lorentz force $\boldsymbol{S}_{\text{EMBr}}$ is then obtained by

$$\boldsymbol{S}_{EMBr} = \boldsymbol{J}\times\boldsymbol{B} \tag{7}$$

At the slide gate inlet, fixed uniform velocites $V_{\text{inlet}} = 1.69$ m/s were applied, based on the steel flow rate (0.007475 m^3/s) divided by the inlet area (0.0044 m^2). The inlet turbulent kinetic energy and its dissipation rate were assumed to be small at 10^{-4} m^2/s^2 and 10^{-5} m^2/s^3. A pressure outlet boundary condition was applied at the domain bottom to include the ferrostatic pressure of the steel (171.5 kPa) based on the distance (2.5 m) below the top surface multiplied by the density and gravity constant. The turbulent kinetic energy and dissipation rate were specified to be 10^{-5} m^2/s^2 and 10^{-5} m^2/s^3 for reverse flow from the bottom boundary, respectively. A free slip boundary condition was applied at the top surface. The WF and NF solidification fronts and SEN walls were no-slip no-penetration walls. The magnetic field was interpolated into the domain based on the measurements shown in figure 1(b).

After the single-phase fluid flow solution was obtained, the Lagrangian DPM tracking and DRW models were used to include the effect of the Ar bubbles on steel flow to correct the flow pattern. The following force balance equation was solved for each individual bubble, of volume V_p.

$$m_\mathrm{p}\frac{\mathrm{d}\boldsymbol{u}_\mathrm{p}}{\mathrm{d}t}=\underbrace{\frac{m_\mathrm{p}18\mu}{\rho_\mathrm{p}d_\mathrm{p}^2}\frac{C_\mathrm{D}}{24}\left(\boldsymbol{u}-\boldsymbol{u}_\mathrm{p}\right)\overbrace{\frac{\rho d_\mathrm{p}\left|\boldsymbol{u}_\mathrm{p}-\boldsymbol{u}\right|}{\mu}}^{\mathrm{Re}_\mathrm{p}}}_{\boldsymbol{F}_D}+\underbrace{0.5m_\mathrm{p}\frac{\rho}{\rho_\mathrm{p}}\left(\frac{\mathrm{D}\boldsymbol{u}}{\mathrm{D}t}-\frac{\mathrm{d}\boldsymbol{u}_\mathrm{p}}{\mathrm{d}t}\right)}_{\boldsymbol{F}_\mathrm{v}}+\underbrace{m_\mathrm{p}\frac{\rho}{\rho_\mathrm{p}}\frac{\mathrm{D}\boldsymbol{u}_\mathrm{p}}{\mathrm{D}t}}_{\boldsymbol{F}_\mathrm{p}}+\underbrace{m_\mathrm{p}\frac{\boldsymbol{g}\left(\rho_\mathrm{p}-\rho\right)}{\rho_\mathrm{p}}}_{\boldsymbol{F}_b} \quad (8)$$

where the four forces are: drag $\boldsymbol{F}_\mathrm{D}$, virtual mass $\boldsymbol{F}_\mathrm{V}$, pressure gradient effect $\boldsymbol{F}_\mathrm{p}$ and buoyancy/gravity $\boldsymbol{F}_\mathrm{b}$. The drag force depends on particle Reynolds number and drag coefficient C_D from Morsi [19]. The first 3 of these forces comprise $\boldsymbol{S}_\mathrm{DPM}$. To save computation time and considering that Ar bubbles < 1 mm comprise <1% of the gas, only large bubbles (1 – 5 mm) were injected and tracked in this two-way coupled calculation. The effect of turbulence on particle dispersion was modeled using the DRW method.

3.3 Bubble Tracking and Capture Model

After solving for the steady multiphase flow fluid using the Eulerian-Lagrangian model, ~2.5 million bubbles were injected into the domain over 60s, and their trajectories tracked for each capture criterion. The number of bubbles injected with diameter d_i, denoted $N(d_\mathrm{i})$, is determined by:

$$N\left(d_i\right)=\frac{3\alpha_i}{4\pi\left(0.5d_\mathrm{i}\right)^3}\cdot\underbrace{\alpha\frac{t_{total}V_cL_t\left(0.5L_w\right)}{1-\alpha}}_{V_\mathrm{g}} \quad \text{where} \quad \alpha_i=\begin{cases}F\left(d_i\right) & i=1\\ F(d_i)-F(d_{i-1}) & i>1\end{cases} \quad (9)$$

where V_g is the total volume of Ar gas injected into half of the caster during the chosen time t_total of 60s; L_t and L_w are the strand thickness and width, respectively; and α is the total Ar volume fraction of 8.2%. The volume fractions of different-size bubbles are denoted α_i , and are based on $F(d_\mathrm{i})$ from equation (2). The advanced force balance capture criterion [10,12] has been validated with plant measurement and exhibited a much better accuracy when compare with simple capture criterion [8], and therefore it was used in this work.

4 Results and discussion

Figure 3 shows the speed just beneath the top surface centerline from the two-way coupled flow pattern. The predicted cross flow from IR toward OR agrees well with the plant measurements, which were even stronger than predicted. Without EMBr, ~500 bubbles were observed in all of the measured sample layers, and only one large bubble (1.4 mm diameter) was observed > 0.5 mm. So, the fraction of all captured bubbles >1 mm, ψ(1 mm), was 0.2% (1/500). The model predicts this value to be 0.3% (432 out of 137372 bubbles), which also matches closely with the plant measurement.

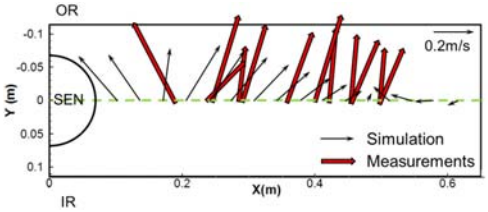

Fig. 3 Velocity on top surface centerline compared with plant nailboard measurements

Flow patterns in the center plane and top surface are shown in figure 4(a) for different EMBr fields. With no EMBr, the nozzle jets impinge on the narrow face, and split, sending some recirculating flow upwards and across the top surface towards the SEN. This is met by flow rising up beside the SEN driven by the buoyancy of the argon gas. Asymmetric swirl caused by the slide gate sends more gas up the inner radius (IR) of the WF, giving complex surface flow with cross flow from IR to OR. With EMBr, the strength of the jet was lessened, and flow in the mid plane changed; small swirls formed just above and below the jet. EMBr also reduced the top surface velocity and lead to more symmetrical top surface flow.

Figure 4(b) shows where small bubbles were captured on the wide face outer radius (WF-OR) with 400 A current in the top coil and 600 A in the lower coil. Many 0.3 mm bubbles were captured near the SEN; fewer bubbles reached the NF region to be captured, especially with a suppressed jet with EMBr. Captured bubbles decrease with distance below top surface. The short black lines show locations of examined sample surfaces.

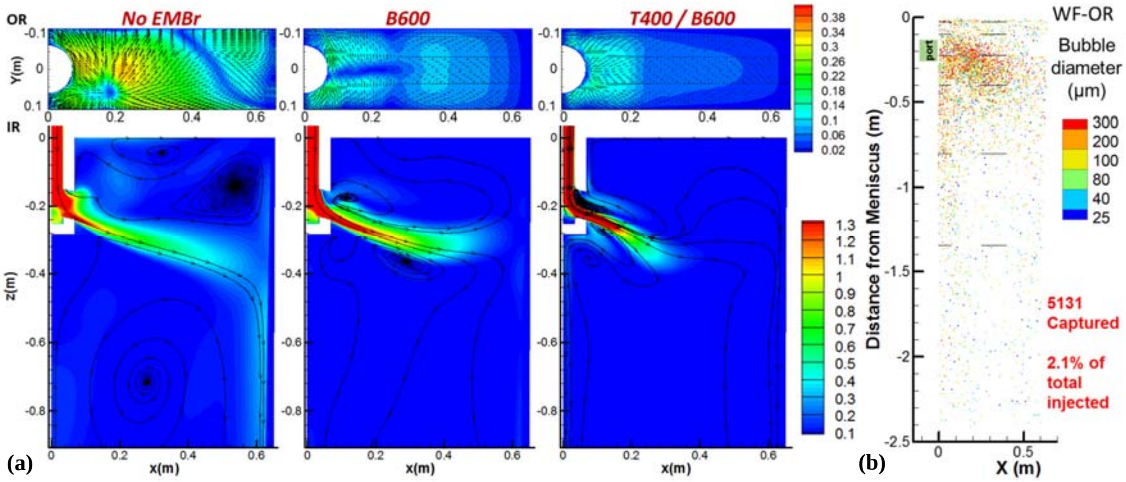

Fig. 4 (a) Velocity magnitude in the midplane and top surface; (b) captured small bubbles with 400 A top coil current and 600 A lower coil current (T400/B600)

The average diameter and number of bubbles predicted to be captured on the examined sample surfaces are compared with measurements in each layer of the plant samples in figure 5(a) and the capture fractions of different bubbles are shown in figure 5(b). Both measurements and numerical model showed the average bubble diameter and bubble size decreasing with distance below top surface. The model underpredicted the number of bubbles captured near the meniscus region, but slightly over predicted the captured bubble size close to the meniscus. With EMBr, the number of bubbles captured near the center region of the top surface was reduced, but no significant difference appeared in the quarter region of the sample.

The capture fractions decrease with bubble diameter. The capture fraction is ~80% for small bubbles (<0.1mm) and less than 0.1% for large bubbles (>1mm). Applying EMBr slightly reduced the capture of small bubbles, but greatly reduced the capture of large bubbles. With EMBr, no bubbles >1mm were captured.

5 Conclusions

The multiphase flow of molten steel, and the transport and capture of argon gas bubbles under different EMBr configurations have been simulated and compared with plant measurement. The two-way coupled Eulerian-Lagrangian model predicts cross flow across the top surface caused by the asymmetrical slide-gate and the argon gas, which agrees well with nailboard measurements. Applying EMBr reduces the penetration of the jet and causes more symmetrical flow in the top surface. EMBr has little effect on the capture fraction of small bubbles (<0.1mm), but it lowers the capture of large bubbles from 0.1% to almost zero.

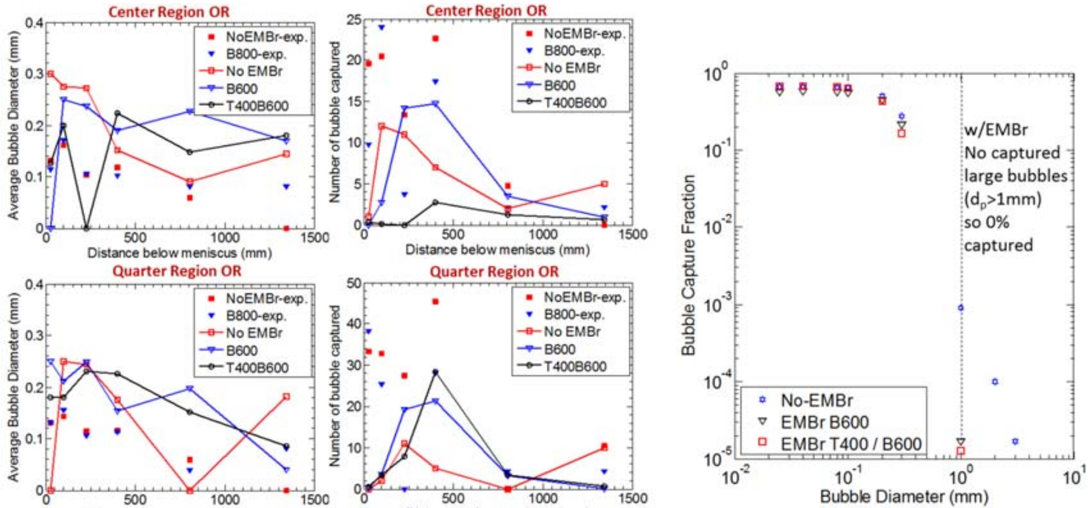

(a) (b)

Fig. 5 (a) Compare predicted captured bubbles in sample with measurements; (b) capture fraction of different bubbles

Acknowledgements: The authors thank Baosteel, Shanghai, PRC, the National Science Foundation (Grant CMMI 11-30882), and the Continuous Casting Consortium, University of Illinois, for support of this project.

References:

[1] Hua Bai and Brian G. Thomas: *Metall. Mater. Trans. B*, 2001, vol. 32, pp. 707–22.

[2] Brian G. Thomas: *Iron Steel Technol.*, 2006, vol. 3, p. 127.

[3] Lifeng Zhang, Jun Aoki, and Brian G. Thomas: *Metall. Mater. Trans. B*, 2006, vol. 37, pp. 361–79.

[4] R. Chaudhary, B. G. Thomas, and S. P. Vanka: *Metall. Mater. Trans. B*, 2012, vol. 43, pp. 532–53.

[5] Ramnik Singh, Brian G. Thomas, and Surya P. Vanka: *Metall. Mater. Trans. B*, 2014, vol. 45, pp. 1098–1115.

[6] Baokuan Li, Toshimitsu Okane, and Takateru Umeda: *Metall. Mater. Trans. B*, 2000, vol. 31, pp. 1491–1503.

[7] B. G. Thomas, X. Huang, and R. C. Sussman: *Metall. Mater. Trans. B*, 1994, vol. 25, pp. 527–47.

[8] K. Jin, B. G. Thomas, R. Liu, S. P. Vanka, and X. M. Ruan: *IOP Conf. Ser. Mater. Sci. Eng.*, 2015, vol. 84, p. 012095.

[9] Quan Yuan, Brian G. Thomas, and S. P. Vanka: *Metall. Mater. Trans. B*, 2004, vol. 35, pp. 703–14.

[10] Quan Yuan: PhD Thesis, University of Illinois at Urbana-Champaign, 2004.

[11] Lifeng Zhang and Yufeng Wang: *JOM*, 2012, vol. 64, pp. 1063–74.

[12] Brian G. Thomas,et al. : *Metall. Mater. Trans. B*, 2014, vol. 45, pp. 22–35.

[13] A. D. Gosman and E. Loannides: *J. Energy*, 1983, vol. 7, pp. 482–90.

[14] Rui Liu, et al.: in *Sens. Sampl. Simul. Process Control*, John Wiley & Sons, San Diego, 2011.

[15] Simon N. Lekakh, et al. : in *2013 AISTech Conf. Proc.*, Association for Iron & Steel Technology, Pittsburgh, PA, 2013.

[16] ANSYS Inc.: *ANSYS FLUENT 12.0 Theory Guide. ANSYS*, ANSYS Inc, 2009.

[17] Paul Rossin and E. Rammler: *J Inst Fuel*, 1933, vol. 7, pp. 29–36.

[18] Brian Edward Launder and D. B. Spalding: *Comput. Methods Appl. Mech. Eng.*, 1974, vol. 3, pp. 269–89.

[19] Saj Morsi and A. J. Alexander: *J. Fluid Mech.*, 1972, vol. 55, pp. 193–208.